PCCP

ROYAL SOCIETY OF CHEMISTRY

PAPER

View Article Online
View Journal | View Issue

Cite this: *Phys. Chem. Chem. Phys.*, 2022, **24**, 24514

An *in situ* study of thermal crystallization of amorphous calcium phosphates†

Lorenzo Degli Esposti,[a] Marco Fosca,[b] Aurélien Canizares,[c] Leire Del Campo,[c] Marco Ortenzi,[b] Alessio Adamiano,[a] Julietta V. Rau[b] and Michele Iafisco*[a]

The heat-induced crystallization of amorphous calcium phosphate (ACP) is an intriguing process not yet well comprehended. This is because most of the works on this topic are based on *ex situ* studies where the materials are characterized after the heat and cooldown cycles, thus missing transient structural changes. Here, we used time-resolved energy dispersive X-ray diffraction and infrared spectroscopy to study, for the first time, the thermal crystallization of ACP *in situ*. The thermal crystallization of two kinds of citrate-stabilized carbonated ACP was studied, as they are promising materials for the preparation of advanced bioceramics. The behavior of these samples was compared to that of two citrate-free ACPs, either doped or non-doped with carbonate ions. Our results evinced that several phenomena occur during ACP thermal annealing. Before crystallization, all ACP samples undergo a decrease in the short-range order process, followed by several internal reorganizations. We have assessed that differently from carbonate-free ACP, carbonated ACPs with and without citrate directly crystallize into a biomimetic poorly crystalline carbonated hydroxyapatite. Citrate-stabilized ACPs in comparison to citrate-free ACPs have a faster hydroxyapatite formation kinetics, which is due to their higher specific surface area. This work reveals the necessity and the potentialities of using *in situ* techniques to effectively probe complex processes such as the heat-induced crystallization of ACPs.

Received 24th May 2022,
Accepted 16th September 2022

DOI: 10.1039/d2cp02352k

rsc.li/pccp

Introduction

Calcium phosphates are excellent materials for application in medicine, agriculture, environmental remediation, cosmetics, catalysis, and many other sectors.[1–3] Their most successful and widespread use is in the form of bioceramics, employed in dentistry and orthopedic surgery.[4] Among calcium phosphate phases, there is renewed interest in the metastable amorphous calcium phosphate (ACP). ACP does not have a precise stoichiometry and is represented by the general formula $Ca_x(PO_4)_y{\cdot}nH_2O$, and it usually consists of rounded nanoparticles containing $Ca_9(PO_4)_6$ clusters surrounded by 3–5 water molecules that "attach" the clusters together.[5] The short-range (local) ordered ACP clusters, defined as Posner's clusters, have a structural similarity to some crystalline calcium phosphates, such as hydroxyapatite (HA, $Ca_5(PO_4)_3(OH)$, Ca/P molar ratio = 1.67) or tricalcium phosphate (TCP, $Ca_3(PO_4)_2$, Ca/P molar ratio = 1.5).[6] ACP has found successful application as a biomaterial for dental remineralization, as a component of self-setting injectable bone cements, and as a coating material of orthopedic prostheses.[7–10] For these applications, the material is used in its amorphous phase, and then it crystallizes, forming the desired crystalline product *in situ*.

Crystallization of ACP is an intriguing process not yet well comprehended and of great relevance for any application. ACP crystallizes both by reacting with water, as well as by heating.[11–13] Thermal crystallization of ACP is a multistep process, which starts with a non-reversible dehydration of its structural water and concludes with the transformation into a crystalline phase, usually occurring in the temperature range between 500 and 800 °C. The thermal crystallization of ACP is thought to be controlled by a solid-state internal lattice reordering mechanism, and usually, the product is TCP, either in the α- or β-form.[7] Previous reports have suggested that the ACP composition, and thus its Ca/P molar ratio, influences the type of crystalline product, usually leading to the formation of mixtures of TCP with other calcium phosphate phases. Recently, we have studied the thermal crystallization of carbonate-doped ACP nanoparticles stabilized by citrate ions (hereafter denoted Cit-ACP). We have

[a] *Institute of Science and Technology for Ceramics (ISTEC), National Research Council (CNR), Via Granarolo 64, 48018 Faenza, Italy. E-mail: michele.iafisco@istec.cnr.it*
[b] *Istituto di Struttura della Materia, Consiglio Nazionale delle Ricerche (ISM-CNR), Via del Fosso del Cavaliere, 100-00133 Rome, Italy*
[c] *CNRS, CEMHTI UPR3079, Univ. Orléans, F-45071 Orléans, France*

† Electronic supplementary information (ESI) available: Chemical composition and SSA_{BET} analysis of ACP samples, the HT-EDXRD patterns of ACP samples at 25 °C and 700 °C, the TD-FTIR spectra of ACP samples at 27 °C, and enlargement of the TD-FTIR spectra in the ranges 800–1200 cm^{-1}, 1200–1700 cm^{-1}, and 480–650 cm^{-1}. See DOI: https://doi.org/10.1039/d2cp02352k

demonstrated that the thermal crystallization of Cit-ACP uniquely leads to the formation of pure HA instead of TCP, as its Ca/P molar ratio (1.70) is closer to the HA's one (1.67).[14] In addition, Cit-ACP was doped with fluoride and carbonate ions, and these ions were maintained in the HA structure formed by heating, allowing the production of a multi-ion doped bioceramic of medical interest.[14]

However, several phenomena may occur to ACP under heating. This is a relevant issue as to the best of our knowledge all the studies on this topic reported in the literature are "*ex situ*", meaning that ACPs were characterized after being heated and subsequently cooled down or quenched to room temperature.[11–13,15–21] Previous *ex situ* studies could have missed transient transformations (*i.e.* very fast-occurring phenomena) such as structural changes occurring during heating or cooling steps.[11–21] So, there is a need for extensive and reliable *in situ* experimental data at high temperatures. For example, *in situ* high-temperature energy dispersive X-ray diffraction (HT-EDXRD) allows observing the processes of crystallization, crystal growth, and changes in crystal phases as a function of temperature.[22–24] Another important technique in this field is the *in situ* temperature-dependent Fourier-transform IR spectroscopy (TD-FTIR) that provides information on the variations in local order that occur in functional groups. TD-FTIR is sensitive to short-range ordered (amorphous) phases and allows discriminating between amorphous and proto-crystalline phases[25,26] as well as studying the thermal stability of volatile substances.[27] Therefore, the aim of this work was to investigate in detail the transformations of Cit-ACP during heating by using complementary HT-EDXRD and TD-FTIR, as these techniques allow the investigation of the heat-induced transformations from the crystallographic point of view as well as at atomic and molecular levels.

From these data, we have evaluated the lifetime of the amorphous phase as a function of temperature, the formation of transient phases, the reaction mechanisms, and the kinetics of HA crystallization, shedding more light on the ACP thermal crystallization process.

Experimental section

Materials

All reagents were purchased from Sigma Aldrich (St. Luis, MO, USA) and were used without purification. Reagents comprise calcium chloride dihydrate ($CaCl_2{\cdot}2H_2O$, $\geq$99.0% pure), hydrochloric acid (HCl, $\geq$37.0% pure), sodium citrate tribasic dihydrate ($Na_3(C_6H_5O_7){\cdot}2H_2O$, $\geq$99.0% pure), sodium phosphate dibasic dihydrate ($Na_2HPO_4{\cdot}2H_2O$, $\geq$99.0% pure), and sodium carbonate monohydrate ($Na_2CO_3{\cdot}2H_2O$, $\geq$99.0% pure). All solutions were prepared with ultrapure water (18.2 MΩ cm, 25 °C, Arium© pro, Sartorius).

Sample preparation

Cit-ACP samples (hereafter denoted Cit-ACP-1 and Cit-ACP-4 as a function of the different nominal Cit/Ca ratio used) were synthesized as reported in the work of Iafisco *et al.*[28] Cit-ACP was prepared by mixing two solutions (1 : 1 v/v, 200 mL total) of (A) 100 mM $CaCl_2$ + *X* mM $Na_3(C_6H_5O_7)$ (where *X* = 100 mM for Cit-ACP-1 and 400 mM for Cit-ACP-4) and (B) 120 mM Na_2HPO_4 + 200 mM Na_2CO_3 under vigorous stirring at room temperature. Before mixing solution (B), pH was adjusted to 9.5 with HCl. After 1 min of stirring, the particles were repeatedly washed with ultrapure water by centrifugation (7000 rpm, 5 min, 4 °C) and then freeze-dried overnight.

Citrate-free ACP samples doped and non-doped with carbonate ions and hereafter denoted Ref-CO_3-ACP and Ref-ACP, respectively, were synthesized by slightly modifying the chemical precipitation described above and used as reference samples. In detail, Ref-CO_3-ACP was prepared by mixing two solutions (1 : 1 v/v, 200 mL total) of (A) 10 mM $CaCl_2$ and (B) 12 mM Na_2HPO_4 + 20 mM Na_2CO_3 at 4 °C, and the precipitate was washed three times by centrifugation (12 500 rpm, 4 min, 4 °C), the first two with water at 4 °C and the last with a solution of ethanol–water (70 : 30 v/v) at 4 °C, and then freeze-dried. Ref-ACP was prepared using a procedure similar to that used for Ref-CO_3-ACP without using Na_2CO_3.

Chemical and crystallographic characterization of ACP samples

Powder X-ray diffraction (PXRD) patterns of the samples were recorded on a D8 Advance diffractometer (Bruker, Karlsruhe, Germany) using Cu Ka radiation, with source parameters set at 40 kV and 40 mA. The patterns were collected in the 2θ range from 10° to 60° with a step size of 0.02° and an acquisition time of 0.5 s.

The Ca and P contents of the samples were measured by using an Agilent 5100 inductively-coupled plasma optical emission spectrometer (Agilent Technologies, Santa Clara, CA, USA). For the analysis, 10 mg of the sample was dissolved in 50 mL of a 1 wt% HNO_3 aqueous solution, and a calibration curve was constructed by using certified standard solutions (Sigma Aldrich, St. Luis, MO, USA). Citrate and carbonate contents were measured through thermogravimetry analysis using an STA 449F3 apparatus (Netzsch GmbH, Selb, Germany). *Ca.* 10 mg of the sample was put in a platinum crucible and heated from room temperature to 1100 °C under air flow at a heating rate of 10 °C min^{-1}; citrate was quantified with the weight loss from 350 to 700 °C and carbonate with the weight loss from 700 to 1000 °C.[28]

The specific surface area (SSA_{BET}) of the samples was measured using a Surfer instrument (Thermo Fisher Scientific, Waltham, MA, USA) through the Brunauer–Emmett–Teller approach for N_2 gas adsorption.

In situ energy dispersive XRD with a controlled temperature program

Data acquisition. EDXRD spectral acquisition was performed at a fixed scattering angle and exploiting the polychromatic radiation of a W-anode bremsstrahlung, performing an energy scan of the diffracted photons. In this way, the fixed experimental setup during acquisition allows a fast, real-time data collection. The EDXRD diffractogram is usually reported as diffracted intensity as a function of the normalized momentum transfer magnitude *q*, where *q* is defined by the formula $q = a \times E \times \sin(\theta)$ ($Å^{-1}$) where *a* is a constant, *E* is the energy of the

specific component of the continuous X radiation and θ is the value of the scattering angle. The energy dispersive diffractogram can be easily converted into an angular one (intensity *vs.* 2θ) by using the given formula. EDXRD patterns were obtained by means of a custom apparatus with a W-anode X-ray tube generating radiation up to 50 keV. Diffracted signals were collected using an EG & G high purity germanium photodiode detector with an energy resolution of 1.5–2.0% in the 20–50 keV range. Upon varying θ, it is possible to modulate the q-range of the collected signal, before data collection with a controlled temperature program, several diffraction spectra have been measured at different values of the scattering angle to individuate the most suitable spectral window (q_{min}–q_{max}) for the analyzed compounds. The operative scattering angle was fixed at a value of $2\theta = 5^\circ$ as the best compromise of possibility to record signals belonging to the initial phase (ACP), the final phase (HA), and the possible transient phases. Maximum radiation energy was set at 50 keV and the current at 30 mA. The EDXRD apparatus was coupled with a customized high-temperature cell (HT-cell) with a PID feedback control system and a dome-shaped beryllium window. The system allowed us to perform high-temperature measurements in the range up to 800 °C. Sample heating was set with a temperature ramp of 5 °C min^{-1} until a temperature of 700 °C. Sample heating and acquisition of diffracted spectra started simultaneously. EDXRD real-time monitoring was performed by acquiring an EDXRD pattern every 2 minutes.

Data processing and analysis. All patterns underwent a smoothing procedure by applying a 5 point adjacent-averaging algorithm. Spectra were plotted and analyzed with the software OriginPro. The HA (211) peak was identified and fitted by using an automated peak fitting routine (OriginPro2016) in order to calculate the peak diffracted intensity as a function of temperature. The following procedure was used: first, the region between 25 and 35 $2\theta^\circ$ was extracted and the baseline of the pattern was removed, then HA (211), (112), and (300) peaks were fitted with a single Gaussian curve, obtaining the (211) peak area as a function of temperature. The HA (002) peak was also identified and fitted by using a similar automated peak fitting routine (OriginPro2016) to calculate the peak full width at half-maximum (FWHM) and peak position as a function of temperature. In this case, the region between 15 and 30 $2\theta^\circ$ was extracted and the baseline of the pattern was removed, then the peak was automatically identified as the 2nd derivative maxima, and finally, it was fitted with a single Gaussian curve obtaining the peak parameters. These parameters were used to calculate the HA crystalline domain along (002) (referred to as $D_{(002)}$) during heating by using Scherrer's formula.

In situ FT-IR spectroscopy with a controlled temperature program

Data acquisition. Infrared spectroscopy has been employed to obtain the reflectance spectra of samples as a function of temperature, in the spectral range from 400 cm^{-1} to 8000 cm^{-1}, with a resolution of 4 cm^{-1}. A Bruker Vertex 80v Fourier Transform Infrared (FTIR) spectrometer equipped with a Bruker Hyperion 3000 microscope has been used for this characterization. The optical configuration included a Globar source, a Ge/KBr beam-splitter, a Cassegrain objective (×15, NA = 0.4), and a liquid nitrogen-cooled MCT detector. A gold mirror was used as a reflectance reference. A TS1500 Linkam heating device, placed on the motion-controlled stage of the microscope, has been employed to heat the sample. In order to obtain kinetic information, a synchronous heating and acquisition method was used. A heating rate of 5 °C min^{-1} was programmed from RT to 700 °C, while a repeated measurement process was performed (2 spectra per min, 64 scans per spectrum). Reference was acquired at the beginning and at the end of the heating process.

Data processing and analysis. Each reflectance spectrum was obtained by computing the ratio between the reflected intensities obtained for the sample and the reference. Finally, for the sake of a better visualization of the structural evolution, all spectra have been normalized to the most intense reflectance value (main PO_4 mode (ν_3)). Normalized spectra were plotted and analyzed with the software OriginPro. The main FTIR peaks (ν_4PO_4, ν_3PO_4, ν_3CO_3, and νCOO) corresponding to the main ACP's chemical species were identified and integrated by using an automated multi-peak analyzer routine (OriginPro2016) to extract the peak full width at half-maximum (FWHM), peak position, and peak area as a function of temperature. The following procedure was used: first, the baseline of each peak was removed, then the peaks were automatically identified as the 2nd derivative maxima, and finally, peaks were integrated, and peak parameters were calculated. This process allowed measuring the variations in peak broadness, position, and area associated with variations in crystallinity, local order, and content of chemical species, respectively, so as to visualize the kinetics of the transformations of ACP during heating.

In addition, the TD-FTIR spectra were further processed to highlight the crystallization of ACP into HA as a function of temperature. In detail, the second derivative of the spectra was calculated by applying the Savitzky–Golay algorithm combined with spectral smoothing to improve the signal-to-noise ratio. Afterward, the second derivative of the spectra was inverted to show the negative peaks.

Results and discussion

Morphological, structural, and compositional characterization of Cit-ACP and Ref-ACP

Cit-ACP and citrate-free ACP samples are amorphous, as shown by their PXRD patterns (Fig. S1, ESI†). Cit-ACP samples were prepared at two different nominal Cit/Ca molar ratios, *i.e.* Cit/Ca = 4 or 1, as reported in our previous works we have found that the Cit/Ca ratio controls their specific surface area (SSA_{BET}) and this, in turn, influences their thermal crystallization as well as the crystallization in water.[14,28] Citrate-free ACPs, used as reference samples, were prepared under similar reaction conditions to those used for preparing Cit-ACPs; however, it should be considered that they cannot be obtained using the same concentration of calcium and phosphate precursors employed for Cit-ACP, as the high supersaturation in the absence of citrate

induces the immediate conversion of ACP into HA (data not shown). Therefore, Ref-CO_3-ACP and Ref-ACP samples were prepared with the same precursor molar ratios of Cit-ACP, but the overall ion concentration was reduced by a factor of 10. Chemical composition and SSA_{BET} values of Cit-ACP samples in comparison with those of citrate-free ACP samples are reported in Table S1 (ESI†). Cit-ACP samples are similar to each other in terms of elemental composition and citrate/carbonate content. Ref-CO_3-ACP has a carbonate content comparable to Cit-ACP samples, while for Ref-ACP, the carbonate content is negligible. The Ca/P molar ratio of Ref-ACP (1.35) matches with the standard value reported in the literature for one common type of ACP (called ACP2, Ca/P = 1.35–1.38).[7] On the other hand, Cit-ACP samples and Ref-CO_3-ACP have higher Ca/P values (1.70 and 1.66, respectively) due to the presence of carbonate ions substituting phosphate ions in the ACP structure, as previously demonstrated by other studies.[11,29] The SSA_{BET} values of all materials are relatively high, as all samples are nanosized. The SSA_{BET} values of Ref-ACP and Ref-CO_3-ACP samples are 50 and 130 $m^2\ g^{-1}$, respectively, which are similar to other ACPs reported in the literature (50–160 $m^2\ g^{-1}$).[30,31] On the other hand, the presence of citrate leads to remarkably higher SSA_{BET} values for Cit-ACP samples, being *ca.* 200 and 300 $m^2\ g^{-1}$ for Cit-ACP-4 and Cit-ACP-1, respectively. Our previous works have shown that the uncommonly high SSA_{BET} values of Cit-ACP are caused by Cit molecules, which adsorb on the surface of ACP nuclei, minimizing their size and increasing their specific surface area.[14,28] In addition, the nominal Cit/Ca molar ratio influences the nucleation lag time, leading to different SSA_{BET} values. As a consequence, the different surface areas influence Cit-ACP crystallization kinetics and thermodynamics.[14,28]

In situ HT-EDXRD analysis of Cit-ACP thermal crystallization

As the first step, the thermal crystallization of ACP samples was investigated *in situ* by using EDXRD coupled with a high-temperature cell.

In Fig. 1, the HT-EDXRD patterns collected during heating of Cit-ACP samples (panels A and B) and citrate-free ACP samples (panels C and D) are presented as three-dimensional graphs together with the corresponding two-dimensional contour plots as well as stack plots in Fig. S2 (ESI†). HT-EDXRD patterns of Cit-ACP samples show that from 30 °C to *ca.* 550 °C both materials remain amorphous, as no diffraction peaks are present and only an ACP characteristic broad band centered around 30° 2θ was detected. In this temperature range, an increase in the intensity of the ACP band can be observed, which can be attributed to the thermal expansion of the sample holder, which is mainly constituted of metal, hence lifting the ACP powder. Consequently, a higher quantity of powder intercepts the incoming X-ray beam and contributes to the diffracted signal. Citrate-free ACP samples have also the same behavior, with a non-specific increase of ACP band intensity between room temperature and 550 °C. In the range between 550 and 700 °C, crystallization occurs in Cit-ACP samples, proved by the progressive formation of several diffraction peaks. This finding is in agreement with our previously reported differential thermal analysis (DTA) data.[14] The crystallization product of Cit-ACP samples is HA as a single phase (PDF card file 00-009-0432) as some of its characteristic peaks can be observed: (002) at 25.6°, the triplets (211), (112), and (300) between 31–33°, respectively, and (310) at 40° (Fig. S3, ESI†). This finding is in agreement with previous *ex situ* analysis.[14] A closer look at high-temperature patterns (Fig. 1 and Fig. S2, S3, ESI†) evidences the formation of another diffraction peak at 35.5° 2θ at temperature >680 °C for both Cit-ACP-1 and Cit-ACP-4, which is attributed to crystalline calcium oxide (CaO, PDF card file 00-037-1497). This peak was expected, as our previous *ex situ* study revealed the formation of a small amount of CaO (less than 1 wt%) due to the reaction between the excess calcium of Cit-ACP (their Ca/P ratio is above 1.67, the stoichiometric value for HA) and atmospheric oxygen during the thermal crystallization.[14] Thanks to this *in situ*

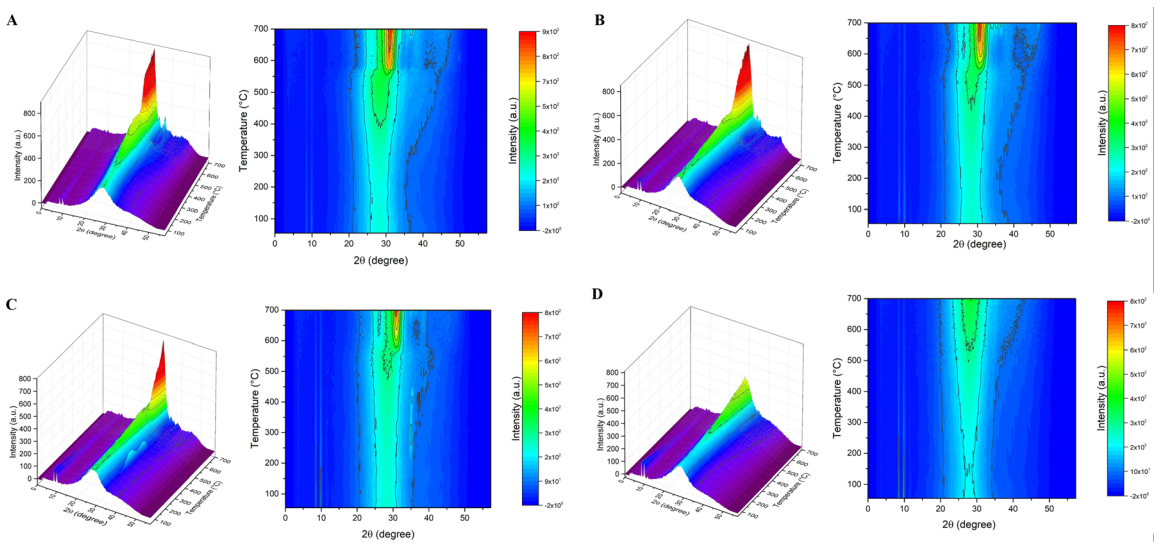

Fig. 1 EDXRD patterns, collected as a function of heating temperature of (A) Cit-ACP-1, (B) Cit-ACP-4, (C) Ref-CO_3-ACP, and (D) Ref-ACP. The two peaks at *ca.* 10° 2θ are due to instrumental contribution and correspond to the anisotropic K_α and K_β fluorescence signals of the W anode tube.

analysis, it has been clarified that CaO formation occurs after Cit-ACP crystallization into HA, and it is not concomitant to crystallization. Interestingly, Ref-CO_3-ACP and Ref-ACP present a different behavior at high temperatures. Ref-CO_3-ACP, similar to Cit-ACP samples, crystallizes into HA (together with traces of CaO), but at a higher temperature (at *ca.* 600 °C) due to its lower surface area. Ref-ACP remains amorphous up to 700 °C, as previously observed by *ex situ* DTA and XRD analyses. Ref-ACP crystallization into TCP occurs at more than 700 °C and could not be observed in our HT-EDXRD experiment.[14] Therefore, these data prove that the chemical composition of ACP controls the nature of the final product obtained by heating.

The HA formation and its crystalline domain dimension were assessed from HT-EDXRD patterns. HA formation was estimated by measuring the intensity of the HA (211) peak (Fig. 2A), as this parameter is proportional to the amount of the crystalline phase. This approach was chosen over other qualitative methods for the evaluation of the degree of crystallinity as the others can be used only for XRD patterns of crystalline materials characterized by several diffraction peaks. This study was carried out only for Cit-ACP samples and Ref-CO_3-ACP, as no crystallization process occurred in Ref-ACP. The data show once again that Cit-ACP samples start to crystallize earlier than Ref-CO_3-ACP (at 530 °C rather than at 570 °C), and the HA phase content increases with heating. The size of the HA crystalline domain along the (002) direction ($D_{(002)}$) as a function of temperature was calculated using Scherrer's equation (Fig. 2B) to estimate the HA crystalline domain dimension along its major *c*-axis. $D_{(002)}$ values show that both Cit-ACP samples and Ref-CO_3-ACP are nanocrystalline, with an average size of *ca.* 5 nm. Interestingly, the size of $D_{(002)}$ does not vary as a function of the temperature up to 700 °C, suggesting that with heating more and more crystalline HA nuclei form without domain size growth.

Overall, our data prove that HA is directly formed through heating of carbonated ACP without the formation of intermediate phases, and rules out the hypothesis that HA is formed by ACP recrystallization during the cooling process. Even if the heating temperature is relatively high and can induce a strong crystal growth, we show that the newly formed diffraction peaks are broad and poorly defined, indicating that HA has nanometric crystalline domains and low crystalline order and that any growth of crystalline domains along the investigated temperature range occurs. This means that the material obtained at high temperature is rather similar to biogenic apatite, which is ion substituted, contains carbonates, and is poorly crystalline.[32] The implication of this finding is that a biomimetic HA ceramic material can be prepared by heating a Cit-ACP precursor.

In situ TD-FTIR spectroscopy of Cit-ACP thermal crystallization

Complementary to HT-EDXRD, TD-FTIR allowed us to investigate the compositional and structural changes that occurred to Cit-ACP samples during heating which are not detectable by XRD. In Fig. 3, the FTIR spectra as a function of temperature for Cit-ACP samples (panels A and B) and citrate-free ACP samples (panels C and D) are represented as three-dimensional graphs together with the corresponding two-dimensional contour plots as well as stack plots in Fig. S4 (ESI†). At room temperature, all samples display the broad absorption bands at *ca.* 560 and 1050 cm^{-1} that are associated, respectively, with the bending (ν_4PO_4) and stretching (ν_3PO_4) modes of phosphate groups in an amorphous environment. In addition, Cit-ACP samples and Ref-CO_3-ACP present additional bands at *ca.* 870 cm^{-1} and in the range 1400–1500 cm^{-1} that were attributed to the carbonate substitution ions inside the ACP structure (ν_2CO_3 and ν_3CO_3 modes, respectively).[33] Finally, Cit-ACP samples present a band at 1560 cm^{-1} that is attributed to the stretching of carboxylate groups of citrate (νCOO).[34] For the sake of clarity, the spectra of the samples recorded before the thermal treatment are reported in Fig. S5 (ESI†). Enlargements of contour plots focusing on phosphate and carbonate bands are provided in Fig. S6–S8 (ESI†).

The TD-FTIR spectra of Cit-ACP-4 and Cit-ACP-1 show that several changes occur during the annealing as shown in Fig. 3 and 4 and Fig. S6–S8 (ESI†) and are summarized in Table 1.

First, from room temperature to *ca.* 120 °C, there is an increase in the ν_3PO_4 band broadness (Fig. S6A and B, ESI†).

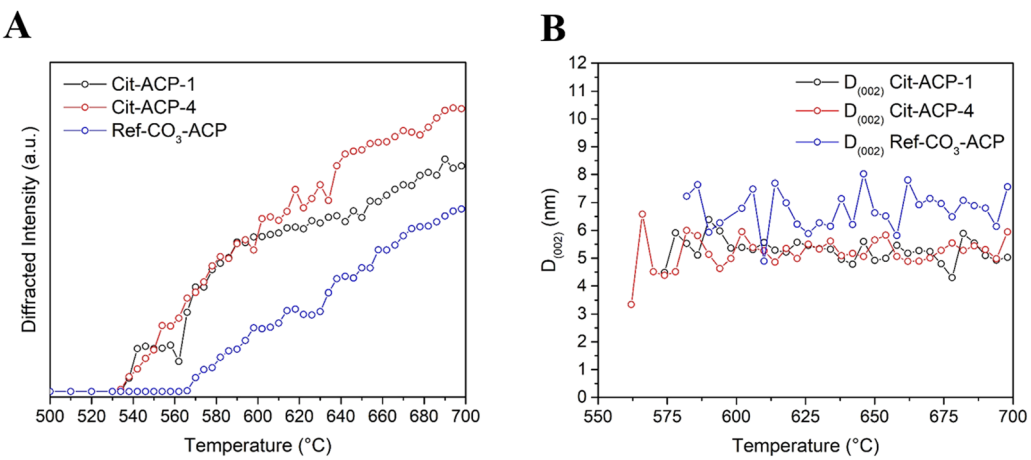

Fig. 2 (A) Diffraction intensity of the (211) HA peak, and (B) HA $D_{(002)}$ size as a function of heating temperature.

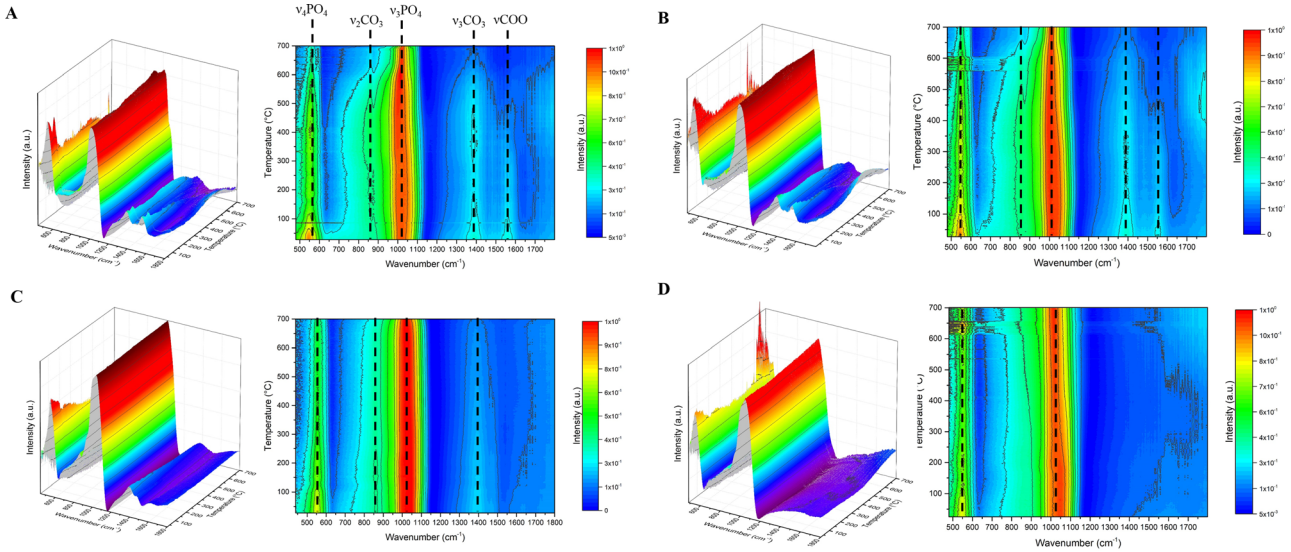

Fig. 3 Normalized TD-FTIR spectra, collected as a function of heating temperature of (A) Cit-ACP-1, (B) Cit-ACP-4, (C) Ref-CO_3-ACP, and (D) Ref-ACP.

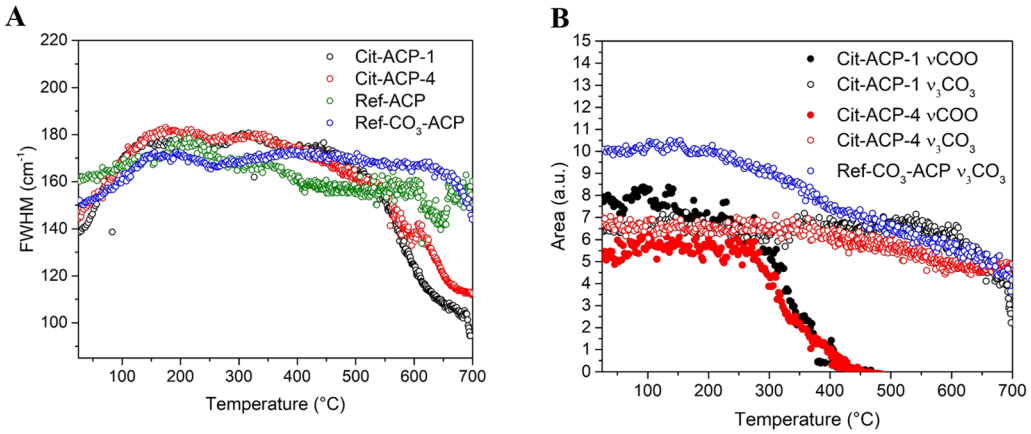

Fig. 4 Results of peak integration analysis. (A) FWHM of the ν_3PO_4 peak, (B) area of νCOO and ν_3CO_3 peaks.

The evolution of band broadness was measured by peak integration analysis, calculating the FWHM of ν_3PO_4 as a function of temperature (Fig. S6A, ESI†). Calcium phosphate bands are constituted by the superposition of several sub-bands associated with P–O vibrations in different local environments.[35] In the case of ACP, the non-ordered structure causes the formation of many different local ionic geometries around phosphate anions, and therefore, their vibrational bands appear broad and without distinctive peaks.[7] Therefore, an increase of FWHM indicates an increment of such distribution (*i.e.* a decrease of short-range order) which can be associated with ACP dehydration, as previously described.[36] No significant differences in ν_3PO_4 FWHM between Cit-ACP-1 and Cit-ACP-4 were observed, suggesting that this event is not influenced by SSA_{BET} of the samples. The increase of FWHM occurs also for Ref-CO_3-ACP and Ref-ACP (Fig. 4A and Fig. S6C and D, ESI†).

Second, from *ca.* 270 to 400 °C, the νCOO band of citrate in Cit-ACP samples decreases in relative intensity in comparison to the ν_3PO_4 band and completely disappears at *ca.* 400 °C (Fig. 4B and Fig. S7, ESI†). This finding confirms that citrate undergoes a thermal decomposition to carbon dioxide before crystallization, as previously suggested by DTA analysis.[14] Also, in this case, the different SSA_{BET} values of Cit-ACP-1 and Cit-ACP-4 do not influence the degradation rate of citrate, as their νCOO area curves are superimposed.

Third, from *ca.* 300 to 500 °C, a redshift of the main phosphate peak ν_3PO_4, with the maximum shifting from *ca.* 1015 to *ca.* 1005 cm^{-1} (Fig. S6A and B, ESI†), was found. This modification can also be observed in Ref-CO_3-ACP and Ref-ACP (Fig. 6C and D, ESI†), but for these samples, it occurs at a lower temperature (between *ca.* 200 and 400 °C) and at different wavenumbers (from 1025 to 1020 cm^{-1} for Ref-CO_3-ACP and from 1030 to 990 cm^{-1} for Ref-ACP). A similar redshift was reported in the literature when other ACPs are heated, and it was tentatively attributed to phenomena associated with dehydration, and to the elimination of voids and the shrinking of

Table 1 Interpretation of the changes in the TD-FTIR spectra of ACP samples as a function of temperature from 25–700 °C

Sample	Temperature range (°C)	Event	Interpretation
Cit-ACP-1	*Ca.* 25–150	Broadening of ν_3PO_4	Decrease of local short-range order[36]
	Ca. 270–400	Decrease of νCOO intensity	Decrease of citrate content
	Ca. 300–500	Redshift of ν_3PO_4 (from *ca.* 1015 to 1005 cm^{-1})	Variation of the local short-range environment (shrinking of volume or change in geometry)[36]
	Ca. 450–550	Deconvolution of ν_2CO_3 from ν_3PO_4 (*ca.* 865 cm^{-1})	Increase of local short-range order
	Ca. 500–600	Narrowing of ν_4PO_4	Increase of long-range order (*i.e.*, crystallization)[36]
	Ca. 530–700	Decrease of ν_2CO_3 and ν_3CO_3 intensity	Decrease of carbonate content
	>570	Splitting of ν_4PO_4 in two bands (560 and 600 cm^{-1})	Formation of an ordered apatitic environment[38]
	Ca. 500–620	Narrowing of ν_3PO_4	Increase of long-range order (*i.e.*, crystallization)[36]
	Ca. 580–620	Blueshift of ν_3PO_4 (from *ca.* 1005 to 1025 cm^{-1})	Variation of the long-range environment[13,36]
Cit-ACP-4	*Ca.* 25–150	Broadening of ν_3PO_4	Decrease of local short-range order[36]
	Ca. 270–400	Decrease of νCOO intensity	Decrease of citrate content
	Ca. 300–500	Redshift of ν_3PO_4 (from *ca.* 1015 to 1005 cm^{-1})	Variation of the local short-range environment (shrinking of volume or change in geometry)[36]
	Ca. 450–550	Deconvolution of ν_2CO_3 from ν_3PO_4 (*ca.* 860 cm^{-1})	Increase of local short-range order
	Ca. 520–650	Narrowing of ν_4PO_4	Increase of long-range order (*i.e.*, crystallization)[36]
	Ca. 530–700	Decrease of ν_2CO_3 and ν_3CO_3 intensity	Decrease of carbonate content
	>620	Splitting of ν_4PO_4 in two bands (560 and 600 cm^{-1})	Formation of an ordered apatitic environment[38]
	Ca. 600–650	Narrowing of ν_3PO_4	Increase of long-range order (*i.e.*, crystallization)[36]
	Ca. 600–650	Blueshift of ν_3PO_4 (from *ca.* 1005 to 1010 cm^{-1})	Variation of the long-range environment[13,36]
Ref-CO_3-ACP	*Ca.* 25–150	Broadening of ν_3PO_4	Decrease of local short-range order[36]
	Ca. 200–400	Redshift of ν_3PO_4 (from *ca.* 1040 to 1020 cm^{-1})	Variation of the local short-range environment (shrinking of volume or change in geometry)[36]
	Ca. 500–700	Decrease of ν_2CO_3 and ν_3CO_3 intensity	Decrease of carbonate content
	>650	Narrowing of ν_3PO_4 and ν_4PO_4	Increase of long-range order (*i.e.*, crystallization)[36]
Ref-ACP	*Ca.* 25–200	Broadening of ν_3PO_4	Decrease of local short-range order[36]
	Ca. 200–400	Redshift of ν_3PO_4 (from *ca.* 1030 to 990 cm^{-1})	Variation of the local short-range environment (shrinking of volume or change in geometry)[36]

the ACP volume.[36] However, this shift can be either a variation of the P–O bond length or a change of phosphate vibrational geometry.[37] Although the interpretation of this redshift is still open, all the hypotheses suggest that with heating, there is a change in the local environment around phosphate groups in all samples before crystallization, and this change occurs at higher temperatures for Cit-ACP samples in comparison to citrate-free ACP ones, independently of the presence of carbonate ions.

Fourth, at around 500 °C, a small peak centered at *ca.* 865 cm^{-1} (for Cit-ACP-1) or 860 cm^{-1} (for Cit-ACP-4) was revealed (Fig. 3 and Fig. S6A, B, ESI†). This peak is the ν_2CO_3 band, and its appearance due to the narrowing of the ν_3PO_4 band indicates a progressive increase of the local order around phosphate and carbonate ions. This suggests that Cit-ACP crystallization occurs through an internal reorganization of ions into a short-range ordered structure; afterward, the apatitic crystallites grow and can be detected by HD-EDXRD. Regarding carbonate bands, there is a slight decrease in the relative intensity and peak area of both ν_2CO_3 and ν_3CO_3 bands between *ca.* 530 and 700 °C (Fig. 4B and Fig. S6, S7, ESI†) that is due to the thermal decomposition of carbonates into CO_2 occurring in parallel with Cit-ACP crystallization. In agreement with our previous DTA data, the amount of this loss is comparable between Cit-ACP-1 and Cit-ACP-4. It is worthy of note that the carbonate bands are still present at 700 °C after the complete crystallization event, confirming that the thermal treatment of Cit-ACP leads to the formation of carbonate-doped HA. The evolution of carbonate bands of Ref-CO_3-ACP as a function of temperature is rather similar to the ones of Cit-ACP samples (Fig. 4B and Fig. S6, ESI†).

Finally, between 500 and 650 °C, the crystallization of Cit-ACP into HA is observed, which is evinced by three main changes to the TD-FTIR spectra. The first is the narrowing of ν_3PO_4 and ν_4PO_4 bands (Fig. 4A and Fig. S6A, B and S8, ESI†). As stated above, for calcium phosphate materials, the FWHM of a peak is inversely proportional to local order, and the narrowing of both phosphate bands indicates the rearrangement of ions in a more ordered (*i.e.*, crystalline) structure as the number of possible geometries around phosphate anions decreases. Interestingly, at 700 °C, the phosphate bands are narrower than the pristine ones but are still relatively broad, suggesting that the final material is poorly crystalline. The second is the splitting of the ν_4PO_4 band into two sub-bands at *ca.* 560 and 600 cm^{-1} (Fig. S8, ESI†). This band deconvolution and structuring into sub-bands indicates that all phosphate ions acquire a precise local environment. In particular, the appearance of two bands at 560 and 600 cm^{-1} for ν_4PO_4 demonstrates that an apatitic crystal structure is obtained, as those are the characteristic ν_4PO_4 frequencies of HA.[38] The last is the blue-shift of the ν_3PO_4 peak from *ca.* 1005 to *ca.* 1025 or 1010 cm^{-1} for Cit-ACP-1 and Cit-ACP-4, respectively (Fig. S6A and B, ESI†). The relationship between ACP crystallization and the blue-shift of the ν_3PO_4 peak to 1010–1020 cm^{-1} is well reported in the literature and described as the formation of an apatitic long-range ordered structure.[13,36]

The crystallization of the samples was also followed by calculating the second-order derivatives of the FTIR spectra, as this mathematical expression allows the magnification of the changes in the ν_3PO_4 position and shape.[39,40] Querido *et al.* have validated the robustness of this data analysis for the study

of ACP-to-HA crystallization in synthetic calcium phosphates, in complex materials such as bones, and in minerals formed in osteogenic cell cultures.[39] In detail, the second-order derivative spectrum of ACP presents a characteristic negative peak at *ca.* 990–996 cm^{-1} while HA or TCP has a corresponding negative peak at 1015–1020 cm^{-1}.[39,40] Second-order derivatives of ACP ν_3PO_4 band are reported in Fig. 5 as three-dimensional graphs together with corresponding two-dimensional contour plots; an enlargement of the 950–1050 cm^{-1} range is provided in Fig. S9 (ESI†). The second-order derivative of Cit-ACP (Fig. 5A, B and Fig. S9A, B, ESI†) clearly shows a negative peak at *ca.* 985 cm^{-1} at room temperature that between 450 and 600 °C shifts to *ca.* 1010–1015 cm^{-1} due to the progressive decrease of ACP and increase of HA.[39] This indicates that in Cit-ACP samples, the phosphate groups initially are in a non-ordered environment, and their transition to an apatitic environment occurs in the 450–500 °C range. Differently, Ref-ACP presents a negative peak at *ca.* 985–970 cm^{-1} which between 400 and 700 °C decreases in intensity without disappearing, while in parallel, a new negative peak at 1000–1020 cm^{-1} appears above 200 °C (Fig. 5C, D and Fig. S9C, D, ESI†). This result suggests that from 200 to 600 °C, a concomitant presence of phosphate ions in a non-ordered local environment and in an ordered environment exists. With heating, a progressive transformation from the former to the latter occurs, and only above 650–700 °C, the ordered environment is predominant. This finding was not observed in previous *ex situ* studies.[40] It is important to mention that for Ref-ACP other crystalline phases could be present, making the second-order derivative analysis difficult to interpret. The second-derivative spectra of Ref-CO_3-ACP (Fig. 5C and Fig. S9C, ESI†) have the features both of the "single peak shift" observed for Cit-ACP samples (*i.e.*, a shift of the maximum between 500 and 650 °C) as well as the "double peak" observed for Ref-ACP (*i.e.*, the permanence of the 985–970 cm^{-1} peak up to 700 °C), suggesting that carbonate ions prevent the early formation of the locally ordered phosphates observed in Ref-ACP.

Associating the crystallization event with the disappearance of the 985–970 cm^{-1} negative peak, the second-order derivative spectra confirm that the crystallization of Cit-ACP samples initiates at lower temperatures (450–500 °C) compared to citrate-free ACP samples (more than 650 °C for Ref-CO_3-ACP, and more than 700 °C for Ref-ACP). The slight discrepancy in the crystallization temperature between HT-EDXRD (from 540–700 °C), TD-FTIR (from 450–500 to 650–700 °C), and our previous DTA analysis (from 500 to 700–800 °C) is due to the experimental setups, as the three setups have different sample holders, sample sizes, mass, volumes, heating systems, and temperature feedback mechanisms, and thus a different heat transfer to the sample.

Overall, the results of TD-FTIR experiments are in good agreement with those of HT-EDXRD and give several additional information on the events that occur in the materials before the crystallization, showing the strength of the technique for this kind of study. In particular, we have discovered that the thermal crystallization of Cit-ACP involves first a loss of order while the material is being dehydrated. This transformation is followed by a rearrangement of phosphate and carbonate ions into a pre-apatitic structure paralleled by citrate decomposition.

By comparing Cit-ACP with its reference samples, we have found that the role of citrate is to delay the first internal rearrangement of phosphate ions and to accelerate the onset of crystallization. It is likely that both effects are caused by the high surface area of Cit-ACP samples. We have also found out that carbonate ions influence the chemical composition (*i.e.*, Ca/P ratio) of ACP, and this in turn leads to the selective

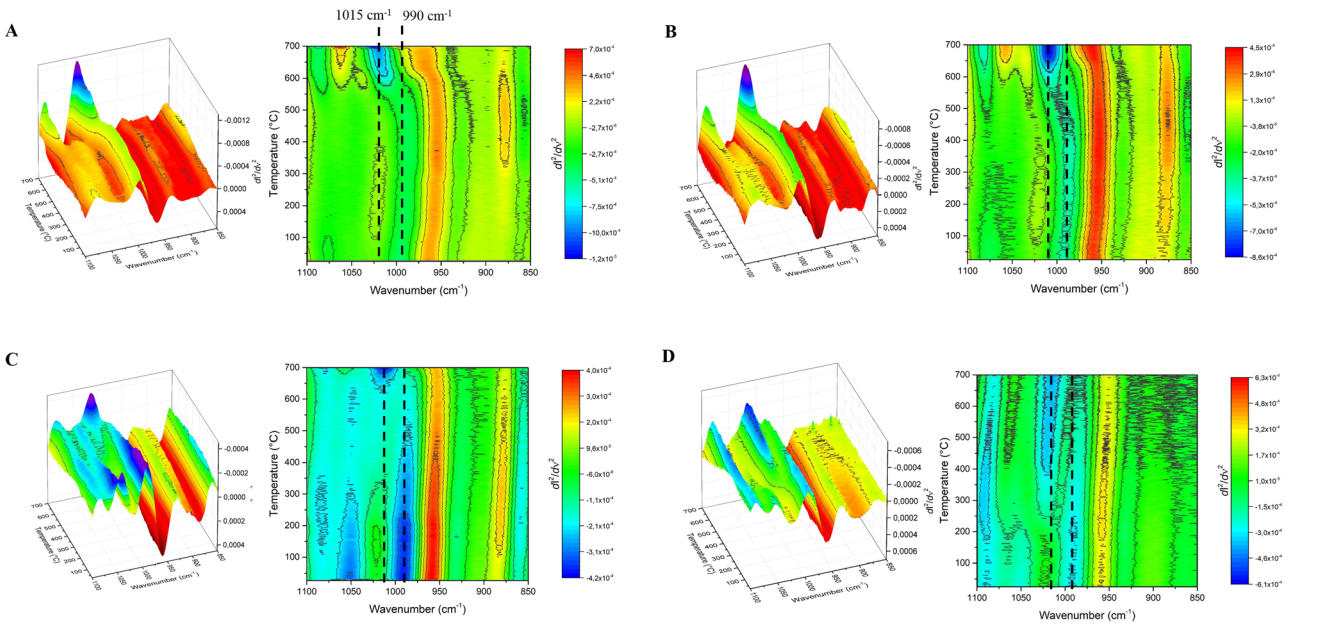

Fig. 5 Second-order derivatives of the TD-FTIR spectra collected as a function of heating temperature of (A) Cit-ACP-1, (B) Cit-ACP-4, (C) Ref-CO3-ACP, and (D) Ref-ACP.

formation of HA instead of TCP. In addition, the use of the second-order derivative on the FTIR spectra suggests that in Cit-ACP samples the transition from the non-ordered local environment to the ordered apatitic environment is discrete, while in citrate-free ACPs, the two local environments (ordered and disordered) coexist for some time. Finally, it must be noted that the TD-FTIR experiment not only shed more light on the thermal crystallization of ACP, but confirmed that the changes in the FTIR spectra observed by *ex situ* works were correctly attributed to the heating process and are not due to the subsequent cooling process.

Conclusions

Our work represents the first *in situ*, real-time study of ACP thermal crystallization using HT-EDXRD and TD-FTIR. We have discovered that several phenomena occur during the heating of ACP, and the crystallization is just the last step of several structural reorganizations. We also found out that citrate and carbonate ions play a critical role in the crystallization kinetics as well as have an effect on the nature of the crystalline product.

This comprehensive investigation of the complex thermal crystallization of ACP paves the way for new research directions in the field. For example, thanks to the knowledge gained from this work, we envision that by using controlled heating of ACP, it will be possible to produce bioactive HA ceramics for medical applications. Indeed, the thermal treatment allows the consolidation of the material, and the use of Cit-ACP as a precursor would allow the improvement of the biomimetism of the ceramic by controlling crystallinity and ion doping. Finally, our work shows the high potentialities of *in situ* techniques that could be used to investigate in depth the crystallization mechanism of other kinds of amorphous materials.

Author contributions

L. D. E.: conceptualization, investigation, visualization, writing – original draft, and writing – review & editing; M. F.: investigation, writing – review & editing; A. C.: investigation, writing – review & editing; L. D. C.: writing – review & editing; M. O.: investigation; A. A.: writing – review & editing; J. V. R.: writing – review & editing; and M. I.: conceptualization, supervision, writing – original draft, and writing – review & editing. All authors have given approval to the final version of the manuscript.

Conflicts of interest

There are no conflicts to declare.

Acknowledgements

This work was supported by the Italian Ministry of Health (Bando Ricerca Finalizzata 2016, no. GR-2016-02364704).

References

1 S. V. Dorozhkin and M. Epple, *Angew. Chem., Int. Ed.*, 2002, **41**, 3130–3146.
2 F. Carella, L. Degli Esposti, A. Adamiano and M. Iafisco, *Materials*, 2021, **14**, 6398.
3 G. Fellet, L. Pilotto, L. Marchiol and E. Braidot, *Agronomy*, 2021, **11**, 1239.
4 N. Eliaz and N. Metoki, *Materials*, 2017, **10**, 334.
5 E. Eanes, *Calcif. Tissue Res.*, 1970, **5**, 133–145.
6 E. Eanes, I. Gillessen and A. Posner, *Nature*, 1965, **208**, 365–367.
7 C. Combes and C. Rey, *Acta Biomater.*, 2010, **6**, 3362–3378.
8 A. Tofighi, P. Chakravarthy, D. Lee, S. Mounic and C. Rey, *Key Eng. Mater.*, 2001, **192**, 769–772.
9 J. Zhao, Y. Liu, W.-B. Sun and H. Zhang, *Chem. Cent. J.*, 2011, **5**, 1–7.
10 L. Degli Esposti and M. Iafisco, *Biomater. Biosyst.*, 2022, **5**, 100037.
11 Y. Li, F. Kong and W. Weng, *J. Biomed. Mater. Res. B*, 2009, **89**, 508–517.
12 L. Sinusaite, A. Kareiva and A. Zarkov, *Cryst. Growth Des.*, 2021, **21**, 1242–1248.
13 V. Uskoković, S. Marković, L. Veselinović, S. Škapin, N. Ignjatović and D. P. Uskoković, *Phys. Chem. Chem. Phys.*, 2018, **20**, 29221–29235.
14 L. Degli Esposti, S. Markovic, N. Ignjatovic, S. Panseri, M. Montesi, A. Adamiano, M. Fosca, J. V. Rau, V. Uskoković and M. Iafisco, *J. Mater. Chem. B*, 2021, 4832–4845.
15 S. Liu, W. Weng, Z. Li, L. Pan, K. Cheng, C. Song, P. Du, G. Shen and G. Han, *J. Mater. Sci.: Mater. Med.*, 2009, **20**, 359.
16 N. Döbelin, T. J. Brunner, W. J. Stark, M. Eggimann, M. Fisch and M. Bohner, *Key Eng. Mater.*, 2009, **396–398**, 595–598.
17 R. Kumar, P. Cheang and K. Khor, *Acta Mater.*, 2004, **52**, 1171–1181.
18 Y. Li, W. Weng and K. C. Tam, *Acta Biomater.*, 2007, **3**, 251–254.
19 M. Maciejewski, T. J. Brunner, S. F. Loher, W. J. Stark and A. Baiker, *Thermochim. Acta*, 2008, **468**, 75–80.
20 S. Somrani, C. Rey and M. Jemal, *J. Mater. Chem.*, 2003, **13**, 888–892.
21 C. Feng, K. Khor, S. Kweh and P. Cheang, *Mater. Lett.*, 2000, **46**, 229–233.
22 J. V. Rau, M. Fosca, V. S. Komlev, I. V. Fadeeva, V. Rossi Albertini and S. M. Barinov, *Cryst. Growth Des.*, 2010, **10**, 3824–3834.
23 J. V. Rau, A. Generosi, V. S. Komlev, M. Fosca, S. M. Barinov and V. R. Albertini, *Dalton Trans.*, 2010, **39**, 11412–11423.
24 M. Fosca, V. S. Komlev, A. Y. Fedotov, R. Caminiti and J. V. Rau, *ACS Appl. Mater. Interfaces*, 2012, **4**, 6202–6210.
25 D. D. S. Meneses, M. Eckes, L. Del Campo, C. N. Santos, Y. Vaills and P. Echegut, *Vib. Spectrosc.*, 2013, **65**, 50–57.
26 Y. Wu, J. Ordonez-Miranda, S. Gluchko, R. Anufriev, D. D. S. Meneses, L. Del Campo, S. Volz and M. Nomura, *Sci. Adv.*, 2020, **6**, eabb4461.
27 J. Zawadzki and M. Wiśniewski, *Carbon*, 2003, **41**, 2257–2267.
28 M. Iafisco, L. Degli Esposti, G. B. Ramírez-Rodríguez, F. Carella, J. Gómez-Morales, A. C. Ionescu, E. Brambilla, A. Tampieri and J. M. Delgado-López, *Sci. Rep.*, 2018, **8**, 17016.

29 Y. Li, D. Li and W. Weng, *Int. J. Appl. Ceram. Technol.*, 2008, **5**, 442–448.
30 J. Vecstaudza and J. Locs, *J. Alloys Compd.*, 2017, **700**, 215–222.
31 R. Sun, M. Åhlén, C.-W. Tai, É. G. Bajnóczi, F. de Kleijne, N. Ferraz, I. Persson, M. Strømme and O. Cheung, *Nanomaterials*, 2020, **10**, 20.
32 J. Gómez-Morales, M. Iafisco, J. M. Delgado-López, S. Sarda and C. Drouet, *Prog. Cryst. Growth Charact. Mater.*, 2013, **59**, 1–46.
33 J. Termine and D. Lundy, *Calcif. Tissue Res.*, 1974, **15**, 55–70.
34 P. Ivanchenko, J. M. Delgado-López, M. Iafisco, J. Gómez-Morales, A. Tampieri, G. Martra and Y. Sakhno, *Sci. Rep.*, 2017, **7**, 8901.
35 C. Rey, O. Marsan, C. Combes, C. Drouet, D. Grossin and S. Sarda, *Advances in calcium phosphate biomaterials*, 2014, 229–266.
36 V. Uskokovic, *Cryst. Growth Des.*, 2019, **19**, 4340–4357.
37 S. R. Ryu, I. Noda and Y. M. Jung, *Appl. Spectrosc.*, 2010, **64**, 1017–1021.
38 A. Antonakos, E. Liarokapis and T. Leventouri, *Biomaterials*, 2007, **28**, 3043–3054.
39 W. Querido, S. Bookbinder, M. C. Oliveira-Nunes, B. Krynska and N. Pleshko, *Analyst*, 2020, **145**, 764–776.
40 V. Uskoković, *Vib. Spectrosc.*, 2020, **108**, 103045.